Eruptive Cycle and Bubble Trap of Strokkur Geyser, Iceland

Eva Patricia Silke Eibl[1], Daniel Müller[2], Thomas R Walter[2], Masoud Allahbakhshi[2], Philippe Jousset[3], Gylfi P Hersir[4], and Torsten Dahm[5]

[1]University of Potsdam
[2]GFZ
[3]GFZ Potsdam
[4]ISOR
[5]GFZ German Research Centre for Geosciences

November 24, 2022

Abstract

The eruption frequency of geysers can be studied easily on the surface. However, details of the internal structure including possible water and gas filled chambers feeding eruptions and the driving mechanisms remain elusive. We recorded eruptions at Strokkur in June 2018 with a multidisciplinary network of seismometers, tiltmeter, video cameras and water pressure sensors to study the eruptive cycle, internal geyser structure and driving mechanisms in detail. An eruptive cycle at Strokkur always consists of 4 phases: the eruption (Phase 1), post-eruptive conduit refilling (Phase 2), gas filling of the bubble trap (Phase 3) and regular bubble migration and implosion at depth in the conduit (Phase 4). For a typical single eruption Phase 1 and 2 persist for 13.1 s. Phase 3 contains a 26.1 s long eruption coda of on average 19 seismic peaks spaced 1.5 s apart generated at 25 to 30 m depth, 13 to 23 m west of the conduit when the bubble trap refills with gas. Phase 4 starts on average 0.9 minutes after the beginning of the eruption and persists for 2.3 min. In this phase on average 8 large bubbles leave the bubble trap and implode at a spacing of 24.5 s at about 7 m depth in the conduit. The duration of the eruption and recharging phase linearly increases with the number of water fountains in close succession (Phase 1), likely due to a larger water, gas and heat loss from the bubble trap and conduit.

Eruptive Cycle and Bubble Trap of Strokkur Geyser, Iceland

Eva P. S. Eibl[1], Daniel Mueller[2], Thomas R. Walter[2], Masoud Allahbakhshi[2], Philippe Jousset[2], Gylfi Páll Hersir[3], Torsten Dahm[1,2]

[1]University of Potsdam, Institute of Geosciences, Karl-Liebknecht-Str. 24-25, 14467 Potsdam, Germany
[2]GFZ German Research Centre for Geosciences, Telegrafenberg, 14473 Potsdam, Germany
[3]ISOR, Reykjavik, Iceland

Key Points:

- Eruptive cycle of Strokkur consists of eruption, conduit refilling, bubble trap gas accumulation and bubble implosions at depth in conduit.
- Duration of phases linearly increases from single to sextuple eruptions, except for the conduit refilling phase.
- We infer a bubble trap at 25-30 m depth 13-23 m west of the conduit feeding single to sextuple eruptions.

Corresponding author: Eva P. S. Eibl, `eva.eibl@uni-potsdam.de`

Abstract

[The eruption frequency of geysers can be studied easily on the surface. However, details of the internal structure including possible water and gas filled chambers feeding eruptions and the driving mechanisms remain elusive. We recorded eruptions at Strokkur in June 2018 with a multidisciplinary network of seismometers, tiltmeter, video cameras and water pressure sensors to study the eruptive cycle, internal geyser structure and driving mechanisms in detail. An eruptive cycle at Strokkur always consists of 4 phases: the eruption (Phase 1), post-eruptive conduit refilling (Phase 2), gas filling of the bubble trap (Phase 3) and regular bubble migration and implosion at depth in the conduit (Phase 4). For a typical single eruption Phase 1 and 2 persist for 13.1 s. Phase 3 contains a 26.1 s long eruption coda of on average 19 seismic peaks spaced 1.5 s apart generated at 25 to 30 m depth, 13 to 23 m west of the conduit when the bubble trap refills with gas. Phase 4 starts on average 0.9 minutes after the beginning of the eruption and persists for 2.3 min. In this phase on average 8 large bubbles leave the bubble trap and implode at a spacing of 24.5 s at about 7 m depth in the conduit. The duration of the eruption and recharging phase linearly increases with the number of water fountains in close succession (Phase 1), likely due to a larger water, gas and heat loss from the bubble trap and conduit.]

Plain Language Summary

[It is easy to study the eruptions of a geyser on the surface. It is however difficult to study the shape of the geyser at depth and the processes that cause eruptions since we cannot observe them directly. Here, we used seismometers, cameras, pressure sensors and one tiltmeter to study the behaviour and area beneath Strokkur geyser, Iceland, in detail in June 2018. We find that the geyser always passes through 4 phases: (i) eruption, (ii) refilling of the conduit with water, (iii) gas accumulation in a bubble trap and (iv) bubbles leaving the bubble trap regularly to implode in the conduit at depth. For single eruptions the eruption and refilling of the conduit last for 13.10 s. The gas refilling in the bubble trap takes place at 25 to 30 m depth, 13 to 23 m west of the conduit and is visible in the seismic data for about 26.1 s. The final phase lasts 2.3 min with on average 8 bubble implosions at a few meters depth in the conduit. During eruptions with multiple water fountains the periods with eruption, gas accumulation and bubble implosions last longer. This is most likely caused by a larger water, gas and heat loss from the system.]

1 Introduction

Around 1000 geysers worldwide (Hurwitz & Shelly, 2017) exhibit spectacular, jetting eruption of hot water (Descloizeaux, 1847). The system is composed of a water-filled reservoir linked to a fresh water supply and heated by a heat source. Geysers typically erupt in regular intervals passing from the end of one eruption to the end of the next one through an eruptive cycle (Wang & Manga, 2010) which is in the range of seconds (Ardid et al., 2019; Munoz-Saez, Manga, et al., 2015) to hours (Han et al., 2013; Vandemeulebrouck et al., 2014; Munoz-Saez, Namiki, & Manga, 2015; Namiki et al., 2014) to months long (Barth, 1940). Eruptive cycles of geysers worldwide can in general be subdivided into eruption, relaxation, recharge and pre-play phase (Munoz-Saez, Manga, et al., 2015; Karlstrom et al., 2013; Kedar et al., 1998; Han et al., 2013; Vandemeulebrouck et al., 2013; Wu et al., 2019; Karyono et al., 2017; Vandemeulebrouck et al., 2014; Ardid et al., 2019; Munoz-Saez, Namiki, & Manga, 2015; Nishimura et al., 2006) (Table 1). However, some geysers do not show these general characteristics (Munoz-Saez, Namiki, & Manga, 2015; Han et al., 2013; Karyono et al., 2017), while other geysers sometimes skip a phase (Kieffer, 1984). It is currently unclear what internal structures such as bubble traps and driving mechanisms might be responsible for regular or irregular eruptions and eruptive cycles. Moreover, the location, depth and number of bubble traps remains mostly elusive.

Geysers with regular eruptive cycles are for example Old Faithful, El Jefe and Lone Star (Kieffer, 1984; Munoz-Saez, Manga, et al., 2015; Karlstrom et al., 2013). Old Faithful, US, is characterised by a 2 or 5 min long eruption (I) followed by a 1 to 3 minute long seismic coda (II) (Kieffer, 1984). Then 0-30 minutes of quiescence (III) are followed by harmonic tremor that increases gradually in intensity and amplitude (IV) before decreasing in the last 5 to 10 minutes (V) before an eruption (I). The total duration of the eruptive cycle follows a bimodal distribution. Munoz-Saez, Manga, et al. (2015) describe the 4 phases at El Jefe, El Tatio, Chile as eruption, relaxation (temperature and pressure drop), recharge and pre-eruptive stage with bubble addition. The eruption lasts on average 51.9 s, the quiescent phase 80.3 s. Karlstrom et al. (2013) report the phases of eruptive cycle at Lone Star geyser, US as 28 min liquid and steam fountaining, 26 min relaxation phase without discharge from the vent, 59 min of recharge in which the geyser refills, 69 min of pre-play with series of 5 to 10 min long pulses of steam-water discharge. While these geysers have a characteristic eruptive cycle, prominent differences are the duration of the cycle (Table 1) and phases, the timing when the conduit refills, and whether the geyser exhibits small eruptions shortly before the main eruption.

The eruptive cycle of a single geyser can also be more chaotic (Munoz-Saez, Namiki, & Manga, 2015; Han et al., 2013; Karyono et al., 2017). Han et al. (2013) characterises the single eruption cycle at cold, CO_2 driven Crystal Geyser, Utah, as composed of 4 phases with two recharge periods. Phase A is 10 to 15 h long and composed of small eruptions (length 7.2 min, spacing 25.2 min). Phase B is a single 0.9 to 1.2 h long, large eruption ending with a drop in water level inside the well and followed by a recharge period. Phase C resembles phase A but is only 5 to 7 h long, while phase D consist of one single, large eruption of 5 to 7 h duration followed by a 10 h recharge period (Han et al., 2013). Lusis', Indonesia, eruptive behaviour consists of 4 phases: (1) regular bubbling activity; (2) clastic geysering; (3) clastic geysering with mud bursts and intense vapour discharge; (4) quiescent phase (Karyono et al., 2017). These phases do not repeat in cyclical order in time.

Partly motivated by incomplete understanding and high level of complexity, experiments at geysers became larger and more multidisciplinary in recent years including instruments such as seismometers, tiltmeters, gravimeters, GPS, lidar, pressure, temperature, acoustic and geochemical sensors, infrared and video cameras and discharge measurements (Dawson et al., 2012; Nishimura et al., 2006; Vandemeulebrouck et al., 2014; Namiki et al., 2014; Wu et al., 2017; Munoz-Saez, Manga, et al., 2015). These multidisciplinary recordings were combined to study the eruptive cycle (Karlstrom et al., 2013; Nishimura et al., 2006; Kedar et al., 1996; Kieffer, 1984; Vandemeulebrouck et al., 2014), the underlying mechanisms driving eruptions (Kedar et al., 1998; Vandemeulebrouck et al., 2014) or the structure, geometry and location of the geyser, its conduit and bubble trap(s) (Nishimura et al., 2006; Kieffer, 1984; Vandemeulebrouck et al., 2014; Wu et al., 2017; Cros et al., 2011; Vandemeulebrouck et al., 2013; Wu et al., 2019; Rudolph et al., 2012; Ardid et al., 2019; Munoz-Saez, Manga, et al., 2015; Munoz-Saez, Namiki, & Manga, 2015; Namiki et al., 2014; Belousov et al., 2013; Walter et al., 2020) (Table 1).

Eruptions of Strokkur geyser, Iceland, and the time period up to 25 s after the eruption were first studied in 1967 (Rinehart, 1968). Seismic signals were discussed and generating processes suggested in these experiments with one single station (Rinehart, 1968; Kieffer, 1984). However, the details of the eruptive cycle and underlying water reservoir system remained elusive. The uppermost part of the conduit has a complex and possibly fracture-controlled conduit geometry as inferred from submerged underwater cameras (Walter et al., 2020). Eibl et al. (2020) monitored the eruptive behaviour of Strokkur over the course of a year, picked 73,466 eruptions and found single to sextuple eruptions whose waiting time after the eruption linearly increased.

To link the surficial observations to processes at depth, here we use a multidisciplinary network of seismometers, tiltmeter, video cameras and pressure sensors (section 3) and the yearly seismic dataset and eruption catalog (Eibl et al., 2020). We describe the eruptive cycle (section 4.1 and 4.2) and seismic source locations (section 4.3) of Strokkur in June 2018. We discuss the eruption (section 5.1), the post-eruptive conduit refilling (section 5.2) and the recharge including gas refilling of the chamber (section 5.3) and bubble implosions at depth in the conduit (section 5.4) in unprecedented detail. We discuss the 4 phases of the eruptive cycle (section 5.5), the mechanism leading to multi-tuple eruptions (section 5.6) and the location of the feeding chamber with respect to the conduit (section 5.7 and 5.8).

2 Field Site of Strokkur Geyser

Strokkur is located in the geothermal valley Haukadalur in southwest Iceland (Fig. 1b). It is a 3 km^2 area of intense thermal spring and geyser activity (Descloizeaux, 1847; Bunsen, 1847) that has been mapped and monitored in the field (Torfason, 1985, 1995) hosting nowadays over 360 hot pots as identified in thermal drone data (Walter et al., 2020).

Nowadays, Strokkur is an episodically erupting geyser with a water filled pool of 12 m diameter on the surface (Rinehart, 1968) which hosts a central about 2.2 m wide conduit (Walter et al., 2020). The system is artesian with constant outflow of water from the pool. While the central conduit is circular on the surface, it narrows down to ∼1.2 m at 5 m depth and is elliptical at ∼9 m depth with an N-S to NE-SW trend inferred to be structurally controlled. At 12 m it widens again and becomes elliptical again at ∼16 to 18 m depth. At a depth of ∼22 m submerged cameras showed a drillhole that released bubbles into the conduit (Walter et al., 2020). This hole was drilled 39.4 m deep in 1963 to reactivate the geyser activity since it became dormant after an earthquake in 1896 (Torfason, 1995, 1985).

Torfason (1995) describe a mean eruption frequency in 1994 of 7 min and an inflow to the geyser of 2 m/s. Newer studies report that Strokkur erupts in eruptions (Fig. 1d) with one to six distinguishable water fountains (Eibl et al., 2020). Water fountains within a multi-tuple eruption are spaced on average 16.1 s apart while the probability for another water fountain is 13.3%. Mean waiting time after single to sextuple eruptions increases linearly from 3.7 to 16.4 min, respectively, while the amplitude or type of the next eruption cannot be predicted (Eibl et al., 2020).

3 Experimental Setup 2018 and Method

We monitored the eruptions of Strokkur from 6 to 10 June 2018 using 2 video cameras, 2 pressure sensors, 5 seismic stations installed at 7 different locations and 1 tilt sensor. Due to tourist activities during daytime and available working agreement, we only recorded during night-time, and de- and re-installed nearby instruments daily. The statistical analysis of eruption intervals over a period of one year in 2017/18 (Eibl et al., 2020) confirmed that eruptions at Strokkur are repeatable. Therefore, recordings from instruments recording at different times can be compared for different eruption types.

3.1 Video Camera, Pressure Sensor and Tilt

Video JVC cameras type GC-PX10 were placed 5 m from the pool and at 40 m distance southeast of the pool to record the bubble growth and water fountain, respectively. Cameras were installed to record video files at 1920x1080 pixels with a temporal resolution of 50 frames per seconds (fps). We used a Sobel edge detection algorithm (Zhang et al., 2009) on the camera data to estimate the height of some eruption fountains (Fig. 1d). The camera was time synchronized by holding a GPS-clock in front of the lens at the beginning and end of each video.

To measure pressure and temperature we placed a diver (Keller DCX 22) inside the pool and one in the outflow channel (Fig. 1). In total we recorded 11.5 h of pressure and temperature data at a sampling rate of 1 Hz. These measurements indicate water level changes associated with different phases of Strokkur.

[h!]

	phase	mean interval	Trap	depth	Reference
Crystal Geyser, US	4	10 h & 32 h			Han et al. (2013)
Old Faithful, US	5	55 m & 75 m	1	20 m, 20 m SW	Kedar et al. (1998); Kieffer (1984); Vandemeulebrouck et al. (2013); Wu et al. (2019
Lusi, Indonesia	4	irregular			Karyono et al. (2017)
Lone Star, US	4	3.2 h	1	10 m, offset	Karlstrom et al. (2013); Vandemeulebrouck et al. (2014)
Calistoga Geyser, US		4.6 m	1	$>$ 42 m	Rudolph et al. (2012)
El Jefe, Chile	4	132 s	1	5-10 m	Ardid et al. (2019); Munoz-Saez, Manga, et al. (2015)
Vega Rinconada, Chile		1.5 h	1	10-15 m	Munoz-Saez, Namiki, and Manga (2015)
El Cobreloa, Chile		13.72 m & 4.67 h	1	300 m	Namiki et al. (2014)
Onikobe, Japan		10 m			Nishimura et al. (2006)
Geyser valley, Russia		bimodal	2+	beneath vent	Belousov et al. (2013)
Great Geysir, Iceland	4	irregular			Barth (1940)
Strokkur, Iceland	4	3.7 m, 6.2 m, 8.8 m 11.3 m, 14.1 m, 16.4 m	1 1+	20-40 m	Eibl et al. (2020)

Table 1. Comparison of geysers worldwide with respect to number of phases in eruptive cycle, eruption interval, bubble trap number, depth of the bubble trap and respective references. For geysers that exhibit changing eruption intervals merely the latest eruption interval is mentioned.

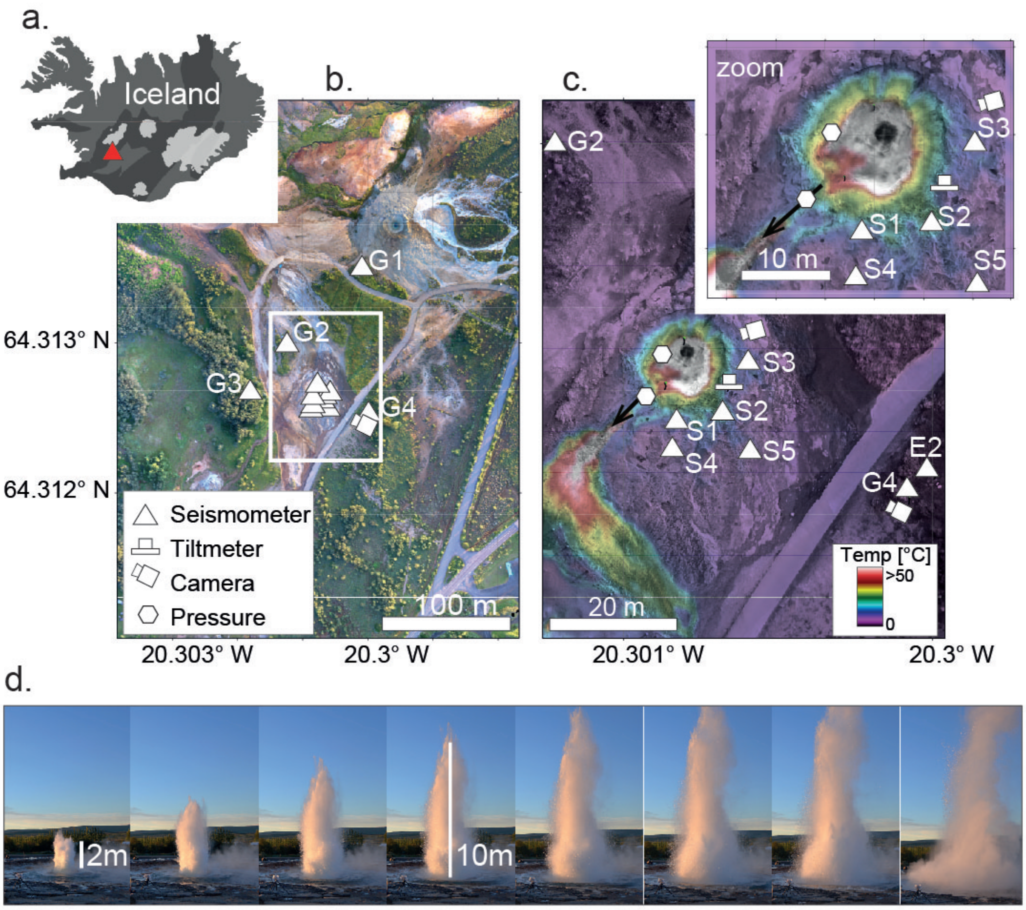

Figure 1. Overview of instrument network around Strokkur geyser. (a) Inset of Iceland with geyser location marked (red triangle), (b) Aerial map generated from camera drone. Symbols indicate instrumentation type and location. (c) Aerial map. Color shading represents thermal infrared pattern (Walter et al., 2020), highlighting the pool and its outflow channel (black arrow). Note location of seismometers (white triangles), cameras (camera symbol), tiltmeter (plate symbol) and pressure-temperature sensors (hexagon symbol), enlarged in upper right insert. (d) The height of the eruption sequence is estimated from video records.

We placed the biaxial platform tiltmeter (Jewell Instr. 701-2(4X)) close to the pool (Fig. 1c). It was oriented with its x axis pointing towards the center of the conduit on the surface and the y axis pointing tangential to it. Data were collected every 0.5 s by the tiltmeter and oversampled by and stored at a rate of 50 Hz at the data cube, with time synchronization by in-built GPS. We lowpass filter the tilt data to 4 Hz before down-sampling to 8 Hz.

3.2 Seismometer

Three Nanometrics Trillium Compact Posthole 20 s broadband seismometers (installed at locations S2, S3, S5, G4) and two Nanometrics Trillium Compact 120 s (installed at locations S1, S4, E2) were linked to data cubes for data collection. S1 to S5 were installed for 4.5 to 5.25 h at 5 to 14 m distance south and east of the pool on the sinter surface (Fig. 1).

The seismic data were detrended, tapered, instrument corrected and filtered. We studied the seismic data with respect to frequency content, amplitude, timing between consecutive eruptions and source location using Python toolboxes (Heimann et al., 2017; Megies et al., 2011).

The covariance matrix of the E, N and Z ground motion was calculated in 1 s long time windows at stations S1 to S5 and G4 (Fig. 1). We calculate eigenvectors and eigenvalues (Bopp, 1992) to approximate the shape of the particle motion ellipse in 3D. The two largest Eigenvalues were used to calculate the linearity of the ellipse: $Lin = 1 - \sqrt{l_2/l_1}$ where eigenvalues $l_1 > l_2 > l_3$. We calculated the azimuth and apparent incidence angle (Bopp, 1992) assuming a radial polarized ground motion according to: $Az = arctan(e_x, e_y)$ and $Inc = arctan(\sqrt{e_x^2 + e_y^2}, e_z)$ where Az and Inc are corrected if $Inc > 90°$ to: $Az' = Az - 180°$ and $Inc' = 180° - Inc$.

In each 1 s long time window we calculate all intersection points of the beams for the five seismometers S1 to S5. We only allowed intersection points in the range of 64.3122 to 64.3136 N and 20.3023 to 20.2997 W. Of all intersection points within that window we calculated the mean and standard deviation. This mean latitude and longitude is defined as the source epicenter. The source depth was estimated from the vertical projection of the epicenter to the linear strokes defined by the incidence angles at each station.

We varied the window length from 0.025 to 2 s and the frequency band in the range 1 to 27 Hz while testing narrow and wide frequency bands. Shorter windows and higher frequencies increased the scatter of the source location in time, but did not lead to more consistent incidence angles. We obtained the best locations in the range from 3 to 9 Hz using a 1 s long time window.

4 Results

4.1 Eruptive Cycle for Single Eruptions

Based on observations from video camera, pressure (Fig. A1), tilt and seismic data (Fig. 2), we characterise a typical eruptive cycle of a single eruption. Duration and amplitude of these observables vary slightly for different eruptive cycles (Fig. A1b). The convention is to use the onset of an eruption as start of an eruptive cycle (Kieffer, 1984).

An eruptive cycle of Strokkur starts with a rising gas bubble that deforms the water surface above the conduit into an about 2 m wide and 40 cm high blue bulge. The bulge becomes white when the rising gas bubble reaches the surface. The bubble surface ruptures, the steam and water mixture jets into the air into a high fountain (Fig. 1c).

At the same time the seismic amplitude increases above the noise level 2-3 s before it peaks and decreases (Fig. 2). During most eruptions the seismic amplitude is increased for less than 5 s and has at 40 m distance energy between 1.2 and 160 Hz (Fig. A2b-f) with most energy around 20 Hz (Fig.2c). The eruption is accompanied by a drop in linearity, azimuths pointing towards the conduit and incidence angles around 90° (Fig. A3).

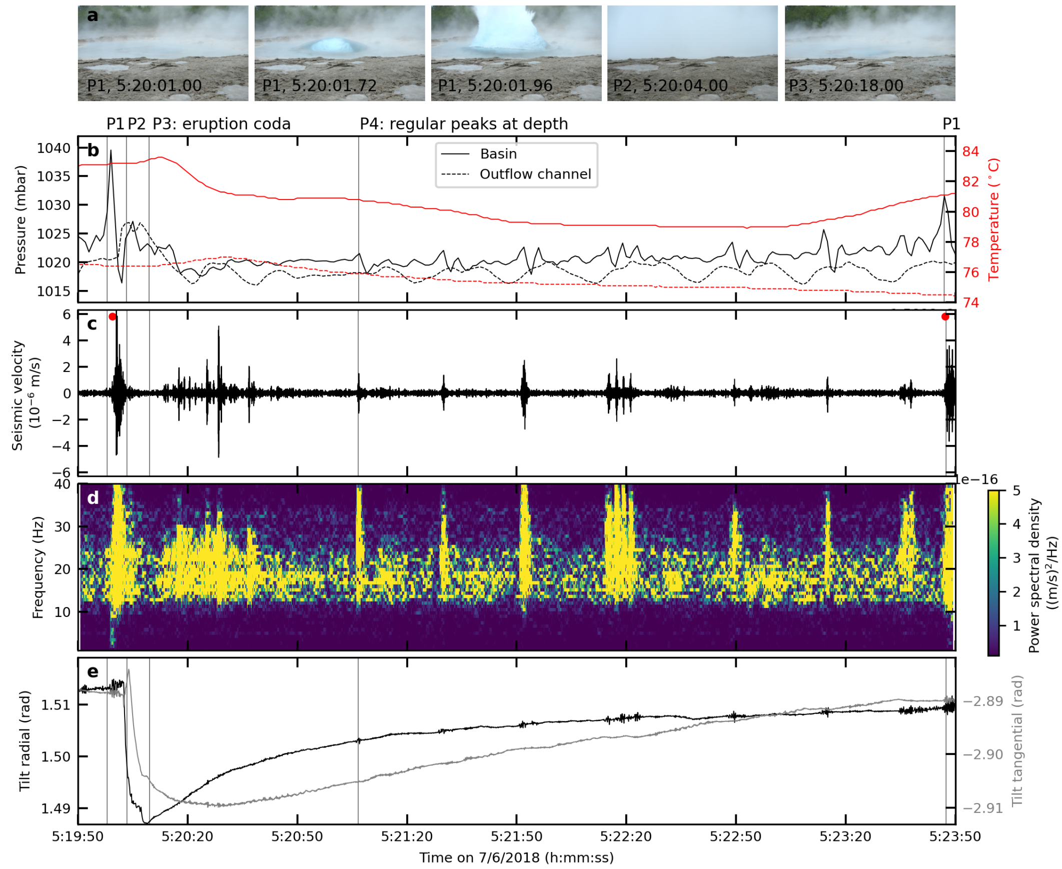

Figure 2. The eruptive cycle of Strokkur on 7 June 2018 from 5:19:50 is subdivided into 4 phases. (a) Photos from Phase 1 (P1), 2 (P2) and 3 (P3). Photos in phase 4 (P4) are similar to Phase 3. (b) Pressure (black) and temperature (red) measured by the pressure sensor in the pool (solid) and outlet (dashed). Phase 1 to Phase 4 marked as P1 to P4, respectively. Grey vertical lines marks start of phases. (c) Vertical seismic ground motion at station E2 filtered 1 to 40 Hz. Red dots mark eruptions as in (Eibl et al., 2020). (d) Spectrogram of subfigure c with 2.56 s window length and 2.28 s overlap. (e) Radial and tangential tilt recorded about 3 m from the pool.

On 7 June 2018 at 5:20:00 both the elevated seismic amplitude and bulge formation and eruption persisted for 2 s. The highest seismic amplitude and broad frequency content correlate with the time of the water fountain.

At 4 m distance east of the pool the radial and transverse tilt signal exponentially increased (Fig. 2d). The frequency content is higher than during the rest of the cycle.

Similarly, the pressure sensor in the pool recorded an exponential increase shortly before an eruption. The eruptions caused a pressure increase of 8 to 32 mbar on 7 June 2018 (Fig. A1) which corresponds to a water wave of 8 to 32 cm height. The pressure sensor in the outlet recorded a broader pressure increase of 3.5 to 10 mbar shortly after eruptions and fluctuations of ±2 mbar between eruptions. The measured temperature peaked at 82 to 87°C about 15 s after the pressure peak.

The water fountain and pool overflow cause a water loss from the pool and conduit while water splashes on the ground (Fig. 1 and 5). Due to a sinter ring around the conduit, the water level in the pool lowered a few centimeters (pressure drop of about 2-3 mbar, Fig. A1a and Fig. 2a) while the water level dropped more than 1 m inside the conduit. However, the conduit refilled within 15 to 20 s (green bar in Fig. A1a) with water from depth, from a shallow aquifer and from the surface flowing back into the pool. This filling is accompanied by a large amount of small bubbles on the surface. In this time period the seismic amplitude is low for about 8 s and the amplitude on the radial and transverse tilt component decreased (Fig. 3 and 2b and c).

Consequently, the tilt signal logarithmic converged towards the original level shortly before the next eruption (Fig. 2d). The first part of this period is characterised by a water filled conduit whose surface is ruptured by a large amount of about 1 cm large bubbles, constant pressure in the pool and the seismic "eruption coda" (Fig. A1). The eruption coda occurs on average 13.10±3.97 s after the beginning of the last water fountain of an eruption (Kieffer, 1984; Eibl et al., 2020). It is dominated by on average 19±4 repeated, regular bursts at a mean spacing of 1.52±0.29 s (Table 2). The temporal spacing increases from 1.5 to 1.6 s in time (Fig. 3g). These bursts have energy between 3 and 71 Hz at 40 m distance southeast of Strokkur with most energy between 10 and 30 Hz (Fig. A2c-e). The amplitude envelope of all events in this phase is asymmetric i.e. the peak amplitude increases fast, then decreases slowly (Fig. 3h) and is visible above the noise level for on average 26.1±6.9 s (Table 2). Azimuths point to a location at depth west of Strokkur with a higher linearity.

While the tilt keeps increasing, the second part of this period is characterised by a calm water surface ruptured by a few cm large bubbles, a slowly rising pressure and water level (cm range) in the pool (Fig. A1a)) intersected by regular peaks in seismic amplitude accompanied by small water level drops in the conduit.

The seismometer recorded on average 8±2 amplitude peaks (Fig. A2c-e) in a 2.3±0.7 min long time interval (Table 2) at a spacing decreasing from 25 to 22 s (Fig. 3a and i). Similarly, the amplitude of the bursts decreases with time towards the next eruption (Fig. 3a). The first seismic amplitude peak occurs on average 0.94±0.19 min after the beginning of a single eruption (Fig. A4). These peaks are shorter in duration than during eruption and have a frequency content of 3 to 160 Hz (Fig. A2). In some cases a short and weak eruption coda is visible.

Times of seismic peaks (located in the conduit at depth) are accompanied by a drop of the water column by a few centimeters inside the conduit, ∼3 mbar pressure peaks and small waves in the pool (Fig. 2 and A1c).

Pressure peaks usually start with a slight positive pulse, followed by a larger negative peak (Fig. A1d). The first derivation of the pressure signal (Fig. A1c) reveals an increasing amplitude of the pressure peaks towards an eruption. However, the last peak before the eruption tends to be smaller while the waiting time after the last visible pressure peak is in a small range of 10 to 20 s.

Based on the characteristics of an eruptive cycle we subdivide it into the 4 phases: Eruption, conduit refilling, eruption coda and regular seismic peaks in the conduit at depth.

	Phase 1-2	Phase 3		
Fig 3a-f (grey points)	Time to start of coda	Number of peaks in coda	Duration coda	Spacing of peaks in coda
single	13.10±3.97 s	19±4	26.1±6.9 s	1.52±0.29 s
double	13.05±2.94 s	36±7	52.4±11.5 s	1.55±0.31 s
triple	13.48±2.88 s	61±14	92.0±22.5 s	1.55±0.30 s
quadruple	13.37±2.51 s	72±19	109.9±30.1 s	1.56±0.30 s
quintuple	14.51±3.38 s	85±19	130.8±30.1 s	1.58±0.34 s
sextuple	12.77 s	142	230.7 s	1.64±0.38 s

	Phase 1-3	Phase 4		
Fig 3a-f (black points)	Time to start of Phase 4	Number of peaks	Duration	Spacing of peaks
single	0.94±0.19 min	8±2	2.3±0.7 min	24.5±5.9 s
double	1.67±0.30 min	11±2	3.8±1.8 min	25.4±6.3 s
triple	2.17±0.47 min	16±3	5.5±1.4 min	23.8±5.6 s
quadruple	2.98±0.54 min	22±6	8.0±2.2 min	24.5±7.0 s
quintuple	3.62±0.36 min	27±5	9.9±2.1 min	23.3±7.2 s
sextuple	4.83 min	29	11.4 min	24.7±8.6 s

Table 2. Characteristics of Phase 1 to 4 for different event types as extracted from Fig. 3a-f. Time to the first peak of eruption coda, duration of eruption coda, number and spacing of peaks in eruption coda, time to first peak in Phase 4, duration of Phase 4 and number and spacing of peaks in Phase 4. Note that 'time to first peak' is measured from the beginning of the last event of a multi-tuple eruption to the first peak in Phase 3 or 4. Values are mean ± 1 standard deviation.

4.2 Eruptive Cycle for Double to Sextuple Eruptions

Double to sextuple eruptions are composed of two to six water fountains at a mean spacing of 16.1±4.8 s, respectively. Measured from the beginning of the last event within an eruption, the waiting time after an eruption increases linearly with the number of water fountains within a multi-tuple eruption (Eibl et al., 2020). The eruptive cycle persists for longer and the system therefore needs longer to recover from a multi-tuple eruption. We note that each eruptive cycle contains all four phases independent of the eruption type where Phase 1, 3 and 4 persist longer for eruptions with higher multiplicity.

The eruption and Phase 1 persist as long as water fountains occur at an average spacing of 16.1±4.8 s (Eibl et al., 2020). The duration of Phase 1 linearly increases from single to sextuple eruptions with 1 to 6 water fountains, respectively. We note that Phase 2 to 4 only follow the last water fountain in a multi-tuple eruption while the first ones are merely followed by another water fountain.

The period from the beginning of the last water fountain within an eruption sequence to the beginning of the coda is constant across all event types and in the range of 12.8 to 14.5 s (Fig. 3 and Table 2). This period includes the last water fountain in Phase 1 and the low seismic amplitude (Phase 2). In double eruptions the first drop in tilt is immediately followed by an exponential increase and a second drop leading to a total larger drop.

The seismic eruption coda in Phase 3 linearly increases in duration from 26.1±6.9 s to 230.7 s while the number of peaks increases from 19±4 to 142 for single to sextuple eruptions, respectively. The mean spacing between the seismic peaks is similar across eruption types and in the range of 1.52 to 1.64 s (Table 2). The peak seismic amplitudes in the eruption coda are slightly larger for eruptions with increasing multiplicity but follow a similar fast increasing, then slowly decreasing amplitude trend (Fig. 3h).

The mean waiting time from the beginning of the last water fountain in an eruption to the first seismic or pressure peak in Phase 4 linearly increases from $0.94{\pm}0.19$ min for single eruptions to 4.83 min for the sextuple eruption (Fig. A4 and Table 2). Phase 4 persists for $2.3{\pm}0.7$ min to 11.4 min (linearly increasing) with $8{\pm}2$ to 29 peaks at a mean spacing in the range of $23.3{\pm}7.2$ s to $25.4{\pm}6.3$ s. The peak spacing at the start of Phase 4 increases from 24 to 28 s for single to quintuple eruption, respectively, while the spacing at the end of the cycle is comparable across eruption types ($\sim$21 s). For all eruption types both the peak spacing and seismic amplitude in Phase 4 decrease with time (Fig. 3i and j).

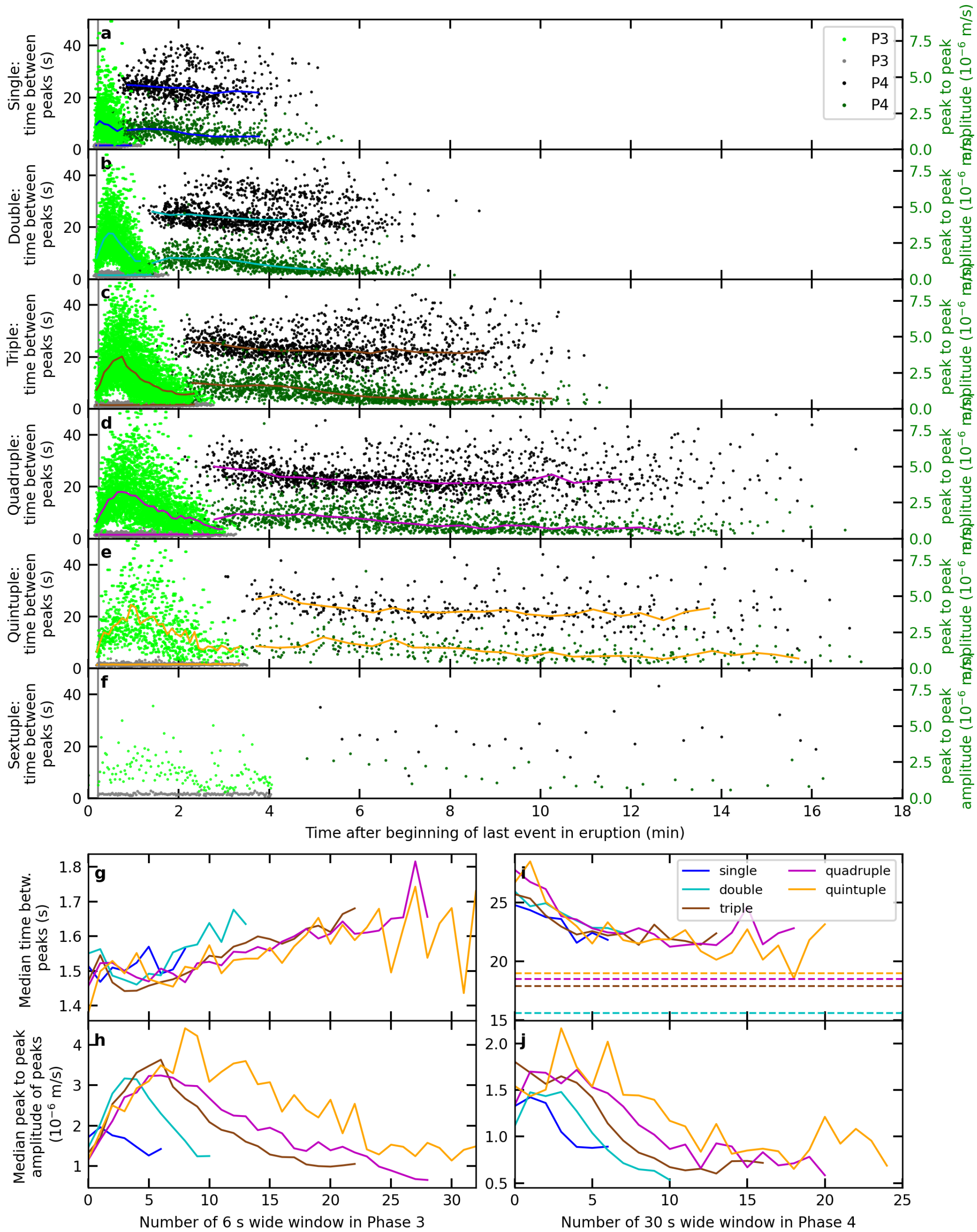

Figure 3. Temporal spacing and amplitude of seismic peaks in Phase 3 and 4 for each eruption type. (a-f) Spacing between peaks in Phase 3 (grey) and 4 (black), amplitude of peaks in Phase 3 (light green) and 4 (green) for (a) 129 single eruptions including the 17 largest, (b) 144 double, (c) 109 triple, (d) 80 quadruple, (e) all 17 quintuple and (f) all 1 sextuple eruptions. Vertical grey line marks onset of Phase 3. Colored lines are medians of each dataset compared across eruption types in subfigure g-j. (g-j) Median spacing and amplitude in time in Phase 3 and 4 for all eruption types. (g) The median temporal spacing and (h) amplitude of peaks in Phase 3. (i) Median temporal spacing and (j) amplitude of peaks in Phase 4. Horizontal dashed lines in (i) mark the spacing between multiple water fountains within a multi-tuple eruption (Eibl et al., 2020).

4.3 Seismic Source Location

Throughout the eruptive cycle most of the seismic signal has a frequency content with most energy between 10 and 30 Hz. During seismic amplitude peaks in Phase 1 and 4 the frequency content is higher with energy up to 71 Hz. Due to stronger attenuation of higher frequencies this may indicate a smaller distance to the seismometer.

The tremor locations resolve two dominant source locations. A deeper tremor source persists in Phase 2 and 3 and most of the time in Phase 4. It peaks at depths of 25 to 30 m and is located 13 to 23 m west of the location of the conduit on the surface (Fig. 4). The tremor is most focused in this region during the eruption coda. This tremor source is characterised by a high linearity.

The second tremor source occurs about half as often and peaks at 8 to 13 m depth (Fig. 4). Its latitude and longitude coincide with the location of Strokkurs' conduit on the surface. The shallow depths correlate with times when either eruptions (Phase 1) or peaks in Phase 4 occur. During peaks in Phase 4, the tremor source is located as shallow as about 5 m (see Discussion on Limitations). These peaks have low linearity on stations S1 and S2 (Fig. A3).

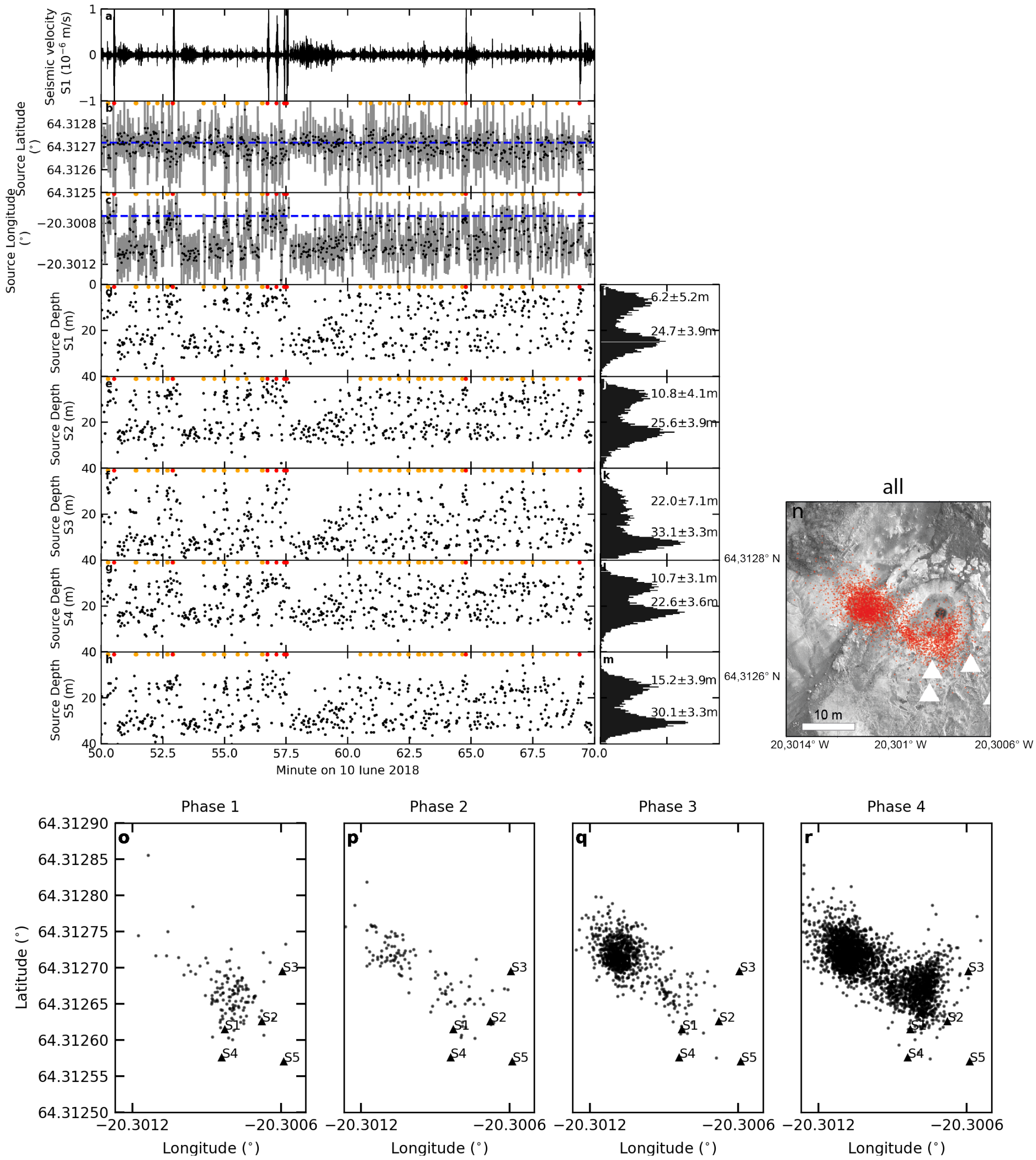

Figure 4. Seismic tremor location on 10 June 2018 in 1 s long time windows filtered 3 to 9 Hz. (a) Seismic velocity seismogram of station S1, (b) Mean latitude and (c) mean longitude for intersection points of beams projected from stations S1 to S5 based on the respective back azimuth. Orange dots mark peaks in Phase 4, red dots mark eruptions. (d-h) Depth derived from mean latitude, mean longitude and incidence angles at station (d) S1, (e) S2, (f) S3, (g) S4 and (h) S5. (i-m) Histograms of subfigures (d-h) with dominant depth ± one standard deviation. (n-r) The best constrained points from subfigure b and c where the standard deviation of the latitude and longitude intersection points was less than the 90% of the mean standard deviation. (n) all and (o-r) sorted according to phases.

5 Interpretation and Discussion

We developed a conceptional structural model of the shallow plumbing system of Strokkur geyser (Fig. 5). It consists of a 35 m long vertical channel with variable cross-section feeding the central surface pool at Strokkur. Hot water continuously drains from the pool through a small trickle. The depth and geometry of the conduit were derived from video camera measurements (Walter et al., 2020). The depth was measured based on the length of the string that was used to move the camera downwards. Depths in the conduit might be overestimated. Based on our tremor locations, our model has at least one sealed bubble reservoir (bubble trap) located at 25 to 30 m depth and 13 to 23 m west of the central pool and its feeder channel.

In accordance with findings at geysers worldwide (Table 1) we subdivide the eruptive cycle of Strokkur into four phases (Fig. 5). These comprise the conduit eruption (phase 1), the refilling of the conduit (phase 2), the gas filling of a bubble trap (phase 3), and bubble flow into the conduit and implosion at depth (phase 4).

We first discuss processes and signals observed during the individual phases, and then compare the structural process model of Strokkur to other geyser models. We finally discuss possible mechanisms leading to single and multi-tuple eruptions.

5.1 Phase 1: Conduit Eruption

The eruptive phase at Strokkur starts when the rising bubble slug approaches the surface and pushes the water column out of the conduit. A blue water bulge forms immediately before the steam jet eruption. Minutes before the bubble bursts, signals such as the decreasing audible and tangible ground motion, the decreasing seismic peak amplitude, the logarithmic converging tilt motion and increasing pressure peaks measured in the pool, were detected. We classify them as long-term eruption precursors. Short-term eruption precursors at Strokkur are in the order of seconds and comprise the increasing seismic amplitude and exponentially increasing tilt signal. We interpret these short-term precursors as caused by the rising slug after it reached the shallowest part of the conduit. It deforms the edifice and generates an increasing seismic noise while it moves towards the surface.

We detect the increasing seismic noise at Strokkur only about 2-3 s before it peaks because the source is too far or too weak to be detected beforehand. This amplitude increase might however also be linked to the widening of the conduit that was inferred from video camera data at a depth of 7 m. James et al. (2006) reported in a laboratory study on a gas slug that acoustic and inertial resonant oscillations can be stimulated by a pressure difference (increase above, decrease below) induced by a gas slug undergoing a change in flow pattern when migrating into a wider conduit.

While water jets into the air, water waves travel from the conduit to the sides of the pool. These waves and the reflected water waves in the pool are detected by the pressure sensor. While water splashes on the ground and generates a chaotic seismic wavefield of white noise for a time period of about 5 s, seismic amplitudes slowly decrease. It is therefore difficult to determine the length of the eruption from the seismic signal. If we discard the shape of the seismic signal caused by an individual water fountain and assess the duration of the total sequence of water fountains, Eibl et al. (2020) found a correlation between eruption duration i.e. number of water fountains and waiting time after an eruption. A similar correlation was found at other geysers (Rinehart, 1965; Azzalini & Bowman, 1990; Namiki et al., 2014; Gouveia & Friedmann, 2006). The tilt and seismic noise short-term precursors are also found at other geysers. However, Kedar et al. (1996, 1998) interpret a seismic signal at Old Faithful that gradually emerged from the white noise (10 Hz to above 40 Hz) as having "no clear precursor". The water falling at Old Faithful lasts 1-3 min (Kedar et al., 1998). Nishimura et al. (2006) recorded a slower, linear increase and uplift on the radial tilt component which started shorty before the eruption of Onikobe geyser reached its end and can therefore be used to predict when the eruption is over and whether the eruption is short or long. Munoz-Saez, Manga, et

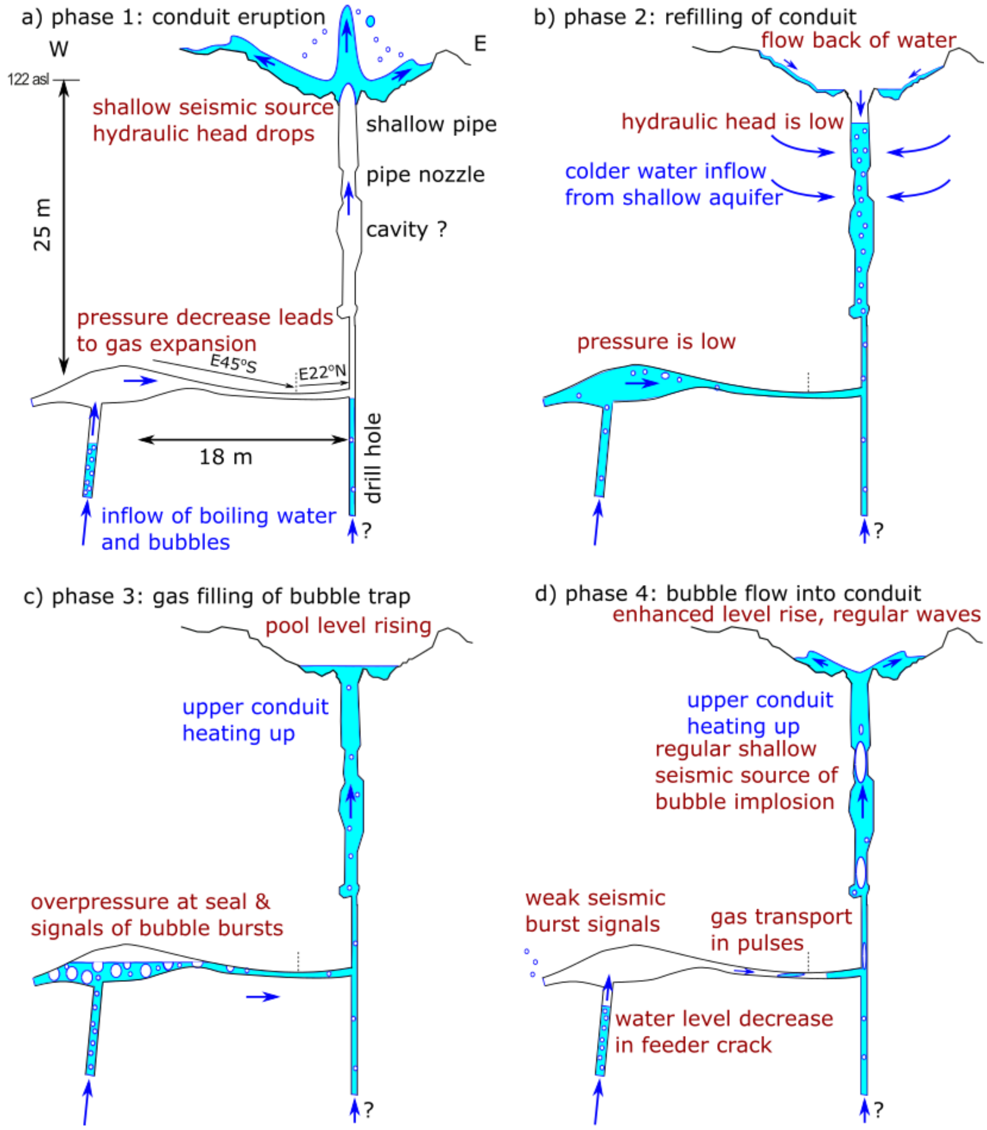

Figure 5. Schematic diagram illustrating conduit and plumbing system of Strokkur geyser and the processes occurring during phases 1-4. The location, geometry and width of the conduit and the sealed bubble reservoir (bubble trap) are based on direct video camera data (Walter et al., 2020) and tremor locations in this study. The eruptive cycle at Strokkur is divided in four phases: (a, phase 1) the eruption, (b, phase 2) the immediate flow back of water and refilling of the upper conduit, (c, phase 3) the gas refilling of the bubble trap reservoir at depth and (d, phase 4) the migration of bubbles from the bubble trap into the conduit and their implosion at depth in the conduit. The observations from different sensors and the hydromechanical processes occurring during each phase are denoted by reddish text.

al. (2015) report that eruptions in El Tatio are accompanied by tilt on both components. Tilt increases in the recharge phase and peaks on the radial component during the eruption potentially due to water ponding in the pool. The tilt drops before the eruption is over, which might be an effect of the water pond and the curve is in general not that steep as at Strokkur. The latter might be caused by a larger distance from the vent in the El Tatio study (Munoz-Saez, Manga, et al., 2015). Tilt at Calistoga Geyser drops after the infrared intensity reached maximum intensity and the geyser erupts (Rudolph et al., 2012). Tilt increased during an eruption of El Cobreloa and decreased slowly afterwards until the next eruption (Munoz-Saez, Namiki, & Manga, 2015). They argue that this reflects recharge in shallow aquifers while increasing tilt as measured near Strokkur or other geysering wells (Nishimura et al., 2006; Rudolph et al., 2012) reflects changes in deeper reservoirs. We infer from our dataset that the eruption releases bubbles from such a deep reservoir.

5.2 Phase 2: Refilling of the conduit

In **Phase 2** Strokkurs' conduit was partly emptied by the eruption, the water is still in the air and splashing back on the ground or is drifting away as steam. While surficial water flows back into the pool and conduit, colder water flows into the conduit from a shallow aquifer and the deep bubble trap is full of hot water flowing in from depth. Strokkurs' conduit refills within about 10 to 15 s.

The temperature in the pool is highest in this period and peaks after the eruption. Our findings contrast Nishimura et al. (2006) who reported a $64°C$ increase in temperature about 50 s before an eruption. The radial tilt signal strongly decreases in Phase 2 and more stongly in double eruptions. Nishimura et al. (2006) interpret such a trend as water removal in the conduit and deep chamber. The seismic amplitude in this time window is low in accordance with the observation that eruptions of Strokkur correlate with seismic signals, that stop before the conduit is refilled (Kieffer, 1984).

This silence might be due to a the gravitational pressure increase in the conduit and plumbing system related to the recovery of the hydraulic head, which suppresses bubble formation at depth. This mechanism has been suggested at Old Faithful geyser (Kieffer, 1984). However, (Kieffer, 1984) report two periods of reduced seismicity of up to a minute in duration during the recharge process. Seismicity is reduced (i) when water rapidly rises in the conduit and the pressure increase suppresses steam bubble formation or (ii) shortly before eruptions when bubbles are in a zone of boiling that is acoustically decoupled from the conduit wall (Kieffer, 1984). Here, we observe only one period of reduced seismicity.

5.3 Phase 3: Gas Filling of the Bubble Trap

In **Phase 3** gradually increasing tilt and linearly increasing pressure in the pool indicate that the water level in the pool gradually rises and the system starts to pressurise at depth. We observe weak and regular seismic peaks (eruption coda), which we associate with bubble bursts at the gas-water contact in the bubble trap. Rising hot water and bubble nucleation in the bubble trap lead to a steadily growing gas volume below the sealing cap of the trap. While gas accumulates and coalesces the gas-water contact migrates downwards in the bubble trap. We speculate that seismic peak amplitudes in this phase increase when the volume of accumulated gas and the temperature in the underlying water increases. The eruption coda ends when the trapped gas has displaced the underlying water into the deeper part of the feeder conduit. The pressure at the gas-water contact is controlled by the hydraulic head in the plumbing system. The pressure at the top of the sealed gas volume, however, is controlled by the vertical height of the gas column and is continuously increasing. We assume that the gas cap in the bubble trap also acts as a temperature barrier, allowing the temperature in the water below the gas cap to also increase and possibly enhance boiling.

Rinehart (1968) reported that the eruption coda at Strokkur consists of 4 to 5 impulsive, mainly upward directed 1 to 2 s long bursts at a spacing of 2 to 3 s in a time interval 9 to 25 s after eruption. Our findings differ since we found 18 to 142 peaks in the eruption coda with energy in both directions (up and down) starting 12.6 to 14.5 s after the beginning of the last water fountain of an eruption sequence. Assuming an eruption duration of less than 5 s, the coda starts about 7 to 9 s after the eruption end and persists more than 25 s. We find that bursts were spaced merely 1.53 to 1.64 s apart and have a duration of less than 1 s. We therefore only agree on the start time of the coda after eruption and the duration of single bursts. The discrepancy in coda duration or burst spacing might be due to a longer time series we analysed or changing behaviour of the geyser.

Rinehart (1968) further reported that within the series of bursts the first 2 to 3 were audible, while we could hear and feel none of the seismic peaks in the eruption coda. Rinehart (1968) attribute the eruption coda to the refilling of underground cavities and slashing of water in a reservoir at depth. They noted that the spacing between these peaks increased in time and interpret it as more slowly moving water splashing from side to side. Here, we confirm this increase in spacing but disagree with the interpretation of water splashing from side to side.

Besides increasing gas volumes or increasing area of the gas-water interface, an increased acoustic impedance mismatch between the water-steam mixture and the conduit walls such as suggested in Kieffer (1984) at Old Faithful, US, might dampen the bursting of these bubbles when the bubble trap is filled with bubbles. Similarly, Kedar et al. (1998) observed a water pressure peak inside the conduit of Old Faithful followed by a seismic peak and therefore link tremor to impulsive events. Tremor increased in amplitude when more impulsive events were present. However, Kedar et al. (1998) also observed that the widening of the conduit during the upwards motion led to a decrease in event number in time while the water level was rising and heat was put in. The tremor amplitude was therefore modulated by the conduit geometry. Here at Strokkur, we do not observe this.

5.4 Phase 4: Bubble Implosions in the Conduit at Depth

The experimental study of Jaupart and Vergniolle (1988) studied rising gas bubbles in a fluid of different viscosities. Bubbles accumulated at the top where the tank was closed apart from a small open conduit. They describe that gas bubbles accumulate and coalesce while part of the foam flowed into the conduit and collapsed on the top. Bubbles coalesce if the foam reaches a critical thickness (dependent on viscosity) and collapse instantly to a single large gas pocket in low viscous fluids. Bubble coalescence and eruption is only possible if foam reaches critical thickness, else there is bubbly flow. The time between two pockets is the time needed to reach the critical thickness again. We presume that Strokkur behaves similarly in Phase 4.

In **Phase 4** the system keeps recharging at depth and bubbles are added to the filled bubble trap. However, first bubbles escape through a narrow crack into the conduit to form a bubble piston. The recordings of a video camera that remained inside the conduit during an eruption indicates that bubbles sometimes implode inside the conduit without reaching the surface (Walter et al., 2020). Bubbles implode at depth if they rise to a cooler and/ or low-pressure area within the water column where the steam condenses (Kedar et al., 1998). At Strokkur bubbles collapse usually with a slight positive pressure peak, followed by a larger negative peak. We observed a first motion during a bubble collapse towards the west, south and down. This suggests that the bubbles implode and free a volume while the water closes in on itself.

Bubble implosions at depth are recorded by acoustic thumps, tangible ground motion up to a few meters distance from the conduit, a drop of the water column in the conduit leading to a sloshing water surface and waves in the pool (Fig. A1d), positive pressure peaks of arriving water waves and 1 s long tilt and seismic amplitude peaks with broad frequency content. These bubble implosions at depth have a weaker eruption coda.

Throughout Phase 4 several bubbles leave the bubble trap and implode at depth in the conduit. The average spacing of 23.3 to 25.4 s (Fig. A1a) is independent of the eruption type. We therefore presume that these gas slugs have the same size across all eruption types. However, the temporal spacing between the implosions decreases and bubble implosions follow more quickly towards the end of Phase 4. This might be due to (i) shorter distance to the collapsing locations, (ii) an increased speed of movement (iii) or faster bubble formation in the bubble trap. A shorter distance to the collapsing location seems unlikely since we expect a bubble to implode at shallower levels towards the end of the eruption when the conduit is hotter. Unfortunately, our seismic network does not allow us to make a statement on relative source depths of bubble implosions within a cycle. We speculate that the bubble moves faster towards the end of the cycle possibly due to an increased temperature in the conduit or a larger vertical dimension of the slug. However, they might also be formed faster in the bubble trap while the temperature increases.

Bubbles might implode (i) at the same location or (ii) at shallower levels. Bubbles could implode at the same depth e.g. after a constriction where pressure drops or in an always colder region of the conduit. If bubbles imploded at the same depth they would need to increase in size to cause larger waves in the pool after implosion. Alternatively, bubbles could reach shallower depths with time as the conduit heats up and allows bubbles to move further before they reach conditions for implosion. Shallower implosions might generate larger waves in the pool as detected by the pressure sensor. (Namiki et al., 2014) suggest that minor eruptions at El Cobreloa, El Tatio heat the conduit and allow major eruptions during which the whole water column in the conduit boils to larger depths. Minor eruptions might correspond to bubble implosions at depth at Strokkur, while major eruptions are similar to eruptions of Strokkur. Here, bubble implosions heat the conduit and hence prepare the system for eruptions.

The seismic signal caused by bubble implosions at depth becomes increasingly weaker throughout Phase 4 until it is neither felt nor heard (Fig. 3). However, they are still inferred visually from the small drop of the water column inside the conduit causing waves in the pool. Both bubble implosions at the same or shallower depth cannot explain this decrease in seismic amplitude. We therefore speculate that the signals are damped when more bubbles exist in the conduit and decouple the bubble noise from the conduit walls. Similarly, in the recharge phase of Old Faithful the amplitude and seismic event rate become stronger and more frequent in time before they become stable (Kedar et al., 1998). However, minutes before the eruption the amplitude drops but event rate remains stable. Periods of reduced seismicity exist up to a minute in duration in the recharge cycle (i) when water rapidly rises in conduit, water squeezes through a narrow area, pressure increases suppresses steam bubble formation (ii) shortly before eruptions when the water-steam mixture is in a zone of boiling that is acoustically decoupled from the conduit wall at the final, steam-rich stages of the eruptive cycle (Kieffer, 1984). At Old Faithful they interpret the drop in seismic amplitude before eruption as more microsteam bubbles which cause an acoustic impedance drop and lead to an inefficient conduction of noise.

The seismic amplitude decrease in Phase 4 of Strokkur contrasts the slowly logarithmic converging radial tilt and pressure signal towards an eruption. The tilt indicates a pressure increase at the cap of the gas reservoir at depth. During this phase, the water level in the pool is linearly increasing, as evidenced by the pressure data measured in the pool. This indicates that water is pushed out the conduit because of the accumulation of bubbles at depth in the bubble trap. Additionally, thermal heating and expansion of the water in the conduit may enhance the water level rise in the pool.

5.5 Eruptive Cycles at Geysers

The eruptive cycle is at most geysers subdivided into the 4 phases eruption, relaxation, recharge and preplay with slowly filling conduits (Kieffer, 1984; Karlstrom et al., 2013). In contrast, Strokkur lacks a preplay phase with small eruptions and merely has bubble implosions at depth in Phase 4. This might be closer to a regular geyser in El Tatio where Munoz-Saez, Manga, et al. (2015) described an eruption, relaxation, recharge of water and bubble adding pre-eruptive stage.

Cycles are mostly (Karlstrom et al., 2013) longer than at Strokkur but sometimes also shorter (Munoz-Saez, Manga, et al., 2015). Geyser such as Old Faithful, US, have a bimodal eruption interval, erupting on average about every 55 or 75 minutes (Kedar et al., 1996). The bimodal distribution is caused by eruptive cycles without seismic quiescence. This contrasts the behaviour of Strokkur where each eruptive cycle contains all 4 phases and the seismic quiescence is the only phase with constant duration across eruption types. The duration of Phase 1, 3 and 4 increases with increasing eruption multiplicity and duration of the eruptive cycle.

5.6 What Causes Multi-tuple Eruptions?

Strokkur is characterised by single to sextuple eruptions. Multi-tuple eruptions are composed of multiple water fountains at an average spacing of 16.1 s, a larger waiting time after eruptions (Eibl et al., 2020), a longer eruption coda, larger amplitude in eruption coda peaks, more bubble implosions at depth and a larger drop in tilt. We propose that more heat, gases and water are lost from the bubble trap during multi-tuple eruptions. This might happen in a bubble trap with rough surface that is fully filled when eruptions are triggered. Since we assume a constant inflow of heat at depth, it takes longer for the system to heat up and pressurize after an eruption with high multiplicity. In a multi-tuple eruption (i) bubbles of similar size might leave the bubble trap in a trail of bubbles and reach the surface if certain conditions are met or (ii) one large bubble leaves the bubble trap and is split into multiple bubbles on the way.

Eibl et al. (2020) reported a mean spacing of water fountains of 15.6±4.5 s to 19.0±5.2 s for single to quintuple eruptions, respectively, with no clear correlation between spacing and eruption type. These values are similar to the spacing between bubble implosions at depth at the end of an eruptive cycle shortly before eruption (Fig. 3i). This might indicate that in multi-tuple eruptions same size bubbles regularly leave the bubble trap and make it to the surface multiple times in a row. Inevitably, shallower and shallower implosion locations throughout the cycle would lead to an eruption. However, if bubbles exploded at the same depth in an area of lower temperature, a closer temporal spacing of bubble implosions might heat this region up shortly and allow bubbles to pass and to reach the surface. In multi-tuple eruptions the spacing of bubbles might have decreased sufficiently to pass this location multiple times before the heat is lost again.

In multi-tuple eruptions a larger part of the bubble trap is emptied, which might lead to a larger bubble migrating into the conduit. To observe multiple water fountains on the surface this large bubble would need to be split into multiple smaller bubbles at a constriction. Contrasting the decreasing temporal bubble implosion spacing in Phase 4, Eibl et al. (2020) reported an increasing spacing between water fountains with time within a multi-tuple eruption. This might support the hypothesis that a larger bubble leaves the bubble trap in a multi-tuple eruption. When it is split into multiple smaller bubbles, later ones might be smaller and travel slower.

5.7 Quality and Limitations of the Tremor Location

An uncertainty of our seismic tremor location using 3 components of a seismometer might be the alignment of the seismometer to geographic north, as compasses are affected by magnetic minerals in volcanic environments. Since S1 to S5 were installed near the geyser on a sinter basement it does not contain a lot of magnetic minerals that affect it. In addition, the azimuths derived during an eruption point towards the location of the conduit on the surface. We are therefore confident that our sensors are not misaligned with respect to geographic north.

We assume a linear wave propagation in a homogeneous medium to locate the source of the seismic tremor. However, we did not convert the apparent incidence angle to real incidence angle. For this correction, a plane wave front is assumed which is most likely not the case at less than 30 m distance from the source. This will lead to a possible overestimation of the tremor source depth.

Based on our waveform analysis we are confident that our seismic source mainly emits P waves. These are characterised by a linear particle motion which we use to point to the source location. Assuming a particle motion parallel to the propagation direction, the back azimuths derived for all 5 stations intersect laterally. We checked for S wave content assuming a particle motion perpendicular to the propagation direction and found that back azimuths no longer intersect. We are at less than 10 m distance from the geyser conduit and further assume that our P wave emitting source at depth does at this distance not create an significant amount of Rayleigh waves. Based on our analysis of the particle motions we are comfortable that we are able to make these assumptions. However, during eruptions the tremor source at Strokkur is dominated by Rayleigh waves. We note that although the eruptions occur on the surface, our source location is not at 0 m depth. This might be because a region down to a few meters is excited. However, since the linearity of the particle motion drops during eruption and Rayleigh waves dominate the waveform, our source depth might also be affected.

While most energy is located in the 10 to 20 Hz frequency band, we use frequencies between 3 and 9 Hz for our source locations. We are able to resolve two clear tremor locations (Fig. 4). We believe that this is not resolvable at lower frequencies due to a lack of energy and at higher frequencies due to increased attenuation and scattering of the waves.

5.8 Depth and Location of the Bubble Chamber

Throughout the cycle there are two different seismic sources present: a (i) stationary, bursting source in the bubble trap at depth with a dominant frequency content between 10 and 30 Hz and (ii) shallow, imploding or bursting seismic source with most energy between 3 and 70 Hz. We assume that the bubbles migrate from a wide bubble trap through a narrow SE-NW oriented crack into a SW-NE oriented fracture into the borehole where they either implode at depth or burst on the surface (Fig 5). The SW-NE oriented fractures are consistent with the dominant fracture pattern in the area (Walter et al., 2020). Similar bubble trap geometries linked via narrow, horizontal cracks to a wider, highly contorted, vertical conduit were mapped in Geyser valley, Kamchatka using video cameras (Belousov et al., 2013).

Based on our locations the cause of the eruptions is not likely to be sudden boiling in the water column that forces hot water upwards. We suggest that the system consists of one large chamber that empties partly in single eruptions, and more thoroughly in sextuple eruptions. There are most probably no separate multiple chambers, unless it is one large connected chamber.

We assume that when the bubbles implode they squeezed through the borehole from the drilling in 1963 since depth locations indicate a depth around 5 m and since video camera observations (Walter et al., 2020) show bubble implosions at less than 18 m depth. This location is beneath stations S1 and S2 that show the most pronounced drop in linearity and change in azimuth (Fig.A3). At Old Faithful Cros et al. (2011) used a Matched Field Processing technique to locate a 10 min long window of regular seismic peaks about 20 min before an eruption at 12 m depth in the conduit. They interpret them as bubble collapses in the water column and report a length of 0.2 s and about 100 events per minute. This spacing is closer to the here reported burst spacing in the eruption coda than the bubble implosions at depth. However, due the fast burst sequence it might also merge into a persistent background tremor if seismometers are far from the source.

Some multidisciplinary studies addressed the number of bubble traps and their depth (Cros et al., 2011; Vandemeulebrouck et al., 2013; Wu et al., 2019; Vandemeulebrouck et al., 2014; Rudolph et al., 2012; Ardid et al., 2019; Munoz-Saez, Manga, et al., 2015; Munoz-Saez, Namiki, & Manga, 2015; Namiki et al., 2014; Belousov et al., 2013). Bubble traps were commonly located at 5 to 40 m depth (Table 1) and in rare cases at larger depth (Rudolph et al., 2012; Namiki et al., 2014). Consistently, we inferred a bubble trap at 25 to 30 m depth.

However, we locate it 13 to 23 m west of Strokkur. The tilt sensor supports this location as both tilt components exponentially increase during eruption, decrease in Phase 2 and increase in Phases 3 and 4. The sensor was therefore not oriented perfectly radial to the pressure source southwest of the geyser conduit at depth. Most publications do not resolve the relative location of the bubble trap with respect to the conduit. However, at Lone Star and Old Faithful, US the reservoir was inferred to be offset to the geyser conduit (Vandemeulebrouck et al., 2013, 2014). Vandemeulebrouck et al. (2013) located bubble collapse signals from 10 to 15 Hz within a 20 m deep, 20 m offset bubble trap, migrating into the conduit in the recharge cycle and exponentially upwards to 10 m depth. Our depth location and lateral offset is also similar to the results of Wu et al. (2017) who located an up to 200 m wide reservoir at 10 to 60 m depth, 100 m southwest of Old Faithful. The conduit is vertical down to a central depth below 15 m, then bends into a horizontal conduit of 20 m length (Vandemeulebrouck et al., 2013) and followed by another vertical continuation down to more than about 80 m from the surface (Wu et al., 2019). The latter could be mapped using 1-5 Hz seismic tremor during the recharge cycle. The feeding system therefore has a constant lateral offset of 20 m to Old Faithful's conduit on the surface. Similarly, Ardid et al. (2019) modelled the seismic broadband deformation caused by El Jefe geyser, Chile and inferred a depth of 10 m and width of 6 m for the bubble trap.

One bubble trap was mostly inferred (Table 1). However, Kieffer (1984) interpreted the two water levels inside the conduit of Old Faithful as two storage regions at 10 to 12 m and 18 to 22 m depth. Nishimura et al. (2006) found a correlation between eruption duration and waiting time afterwards. Since the long waiting times randomly shortened without any systematic pattern, they interpreted it as two bubble chambers beneath the vent. Based on our tremor location we suggest one bubble trap feeding all eruption types at Strokkur and similar mechanisms driving single to sextuple eruptions.

6 Conclusion

We recorded the eruptive cycle of Strokkur geyser with a multidisciplinary network of seismometers, pressure sensors, video cameras and one tiltmeter. The pressure, tilt and seismic sensors allowed us to investigate processes at depth. These processes were linked through the water column to the surficial water changes recorded by the pressure sensors and cameras. Processes from depth unveil themselves as bubbling, thumps and slight ground shaking or even sloshing water surface and water level drops at the surface.

Depending on the eruption type, eruptions occur every 3.7 to 16.4 min (Eibl et al., 2020). Here we found that all eruptive cycles consist of 4 phases: eruption, refilling of the upper conduit, refilling of the bubble trap and thermal input by bubble implosions in the conduit at depth. Eruption, recharge and bubble implosions at depth persist longer in a longer eruptive cycle but are inherently similar in characteristics. We therefore conclude that all eruption types are fed from the same reservoir and mechanisms. We located this bubble trap at 25 to 30 m depth, 13 to 23 m west of the conduit. Bubbles leave this bubble trap as a trail of bubbles and burst at 7 m depth until pressure and temperature conditions allow them to make it to the surface and burst in a water fountain persisting for a few seconds (Fig. 5). We conclude that, although in past decades Strokkur was artificially changed by drainage and drilling, its driving system is controlled by complex natural conduit and reservoir geometries at depth.

Acknowledgments

We thank the Environment Agency of Iceland and the National Energy Authority for the research permit at the Geysir geothermal field and the rangers for guidance and support. We thank the Geophysical Instrument Pool Potsdam (GIPP) for the instrument loan. This work was financially supported by a GFZ expedition grant and VOLCAPSE, a research project funded by the European Research Council under the European Union's H2020 Programme/ERC Consolidator Grant [ERC-CoG 646858] and the Daimler Benz Foundation (32-02/18). Seismic data of this Strokkur experiment are available through GEOFON $http://doi.org/10.5880/GFZ.2.1.2019.005$. We thank Magnus T. Gudmundsson, Heiko Woith, Tanja Witt for support in the field, Sharon Kedar for feedback and Jonas Schmidt and Shaig Hamzaliyev for bubble burst and implosion picking and method approval.

Appendix A Appendix

References

Ardid, A., Vera, E., Kelly, C., Manga, M., Munoz-Saez, C., Maksymowicz, A., & Ortega-Culaciati, F. (2019). Geometry of Geyser Plumbing Inferred From Ground Deformation. *Journal of Geophysical Research: Solid Earth*, *124*(1), 1072–1083. doi: 10.1029/2018JB016454

Azzalini, A., & Bowman, A. W. (1990). A look at some geyser data from Old Faithful geyser. *Appl. Statist.*, *39*(3), 357–365.

Barth, T. F. W. (1940). Geysir in Iceland. *American Journal of Science*, *238*(6), 381–407.

Belousov, A., Belousova, M., & Nechayev, A. (2013). Video observations inside conduits of erupting geysers in Kamchatka, Russia, and their geological framework: Implications for the geyser mechanism. *Geology*, *41*(4), 387–390. doi: 10.1130/G33366.1

Bopp, M. (1992). *Kombinierte Polarisations- und Arrayanalyse seismischer Daten aus dem Umfeld der Kontinentalen Tiefbohrung* (Unpublished doctoral dissertation). Ludwig-Maximilians-Universität München.

Bunsen, R. (1847). Über den inneren Zusammanhang der pseudovulkanischen Erscheinungen Islands. *Wöhlers und Liebigs Annalen der Chemie und Pharmacie*, *LXII*, 1–59.

Cros, E., Roux, P., Vandemeulebrouck, J., & Kedar, S. (2011). Locating hydrothermal acoustic sources at Old Faithful Geyser using Matched Field Processing. *Geophysical Journal International*, *187*(1), 385–393. doi: 10.1111/j.1365-246X.2011.05147.x

Dawson, P. B., Benítez, M. C., Lowenstern, J. B., & Chouet, B. A. (2012). Identifying bubble collapse in a hydrothermal system using hidden Markov models. *Geophysical Research Letters*, *39*(1), 1–5. doi: 10.1029/2011GL049901

Descloizeaux, A. (1847). LX. Physical and geological observations on the principal Geysirs of Iceland. *The London, Edinburgh, and Dublin Philosophical Magazine and Journal of Science*, *30*(203), 391–409. doi: 10.1080/14786444708645417

Eibl, E. P., Hainzl, S., Vesely, N. I. K., Walter, T. R., Jousset, P., Hersir, G. P., & Dahm, T. (2020). Eruption Interval Monitoring at Strokkur Geyser, Iceland. *Geophysical Research Letters*.

Gouveia, F. J., & Friedmann, S. J. (2006). *Timing and prediction of CO2 eruptions from Crystal Geyser, UT* (Tech. Rep.). Lawrence Livermore National Laboratory. doi: 10.2172/897988

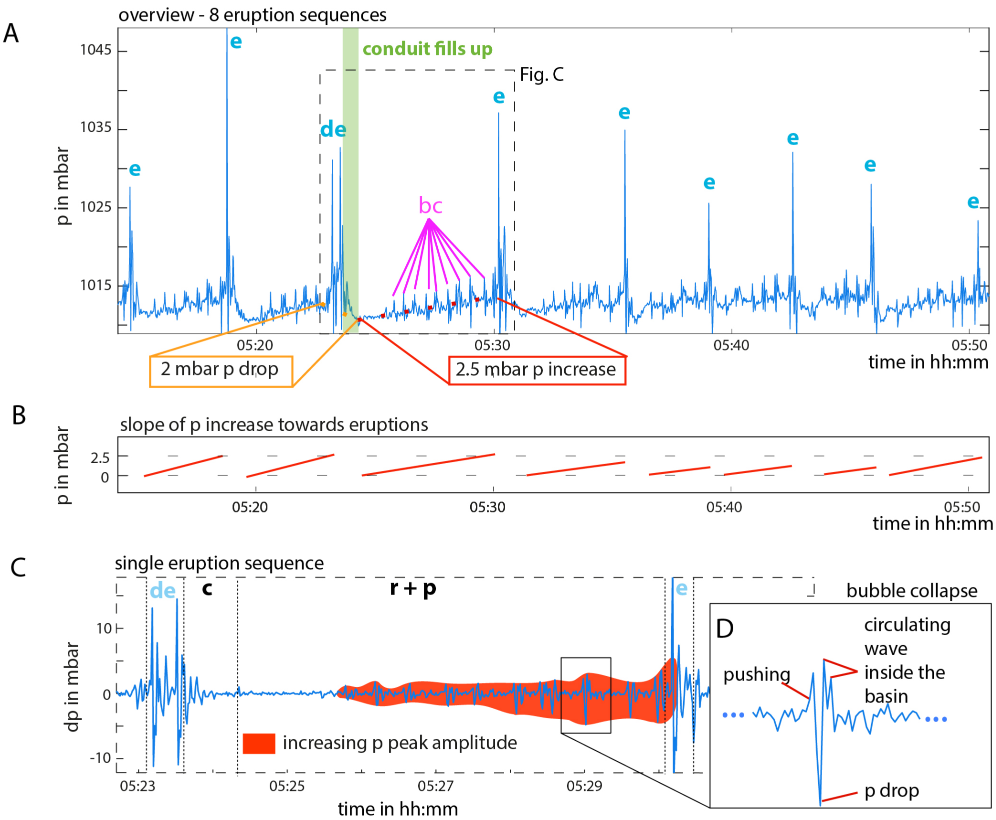

Figure A1. Pressure sensor recordings. (a) Sequence of 8 eruptions, demonstrating the typical observations at the pressure sensor inside the geyser pool. Eruptions are marked by e, double eruptions by de. Peaks in pressure are marked by bc (magenta). The pressure data revealed a certain range of pressure conditions in the pool, that are affecting and affected by the eruptive behavior, like pressure drop during and increase after eruptions. (b) Pressure increase at the sensor, the water level changes respectively, which slightly varies in amplitude and frequency from cycle to cycle. (c) (zoom of subfigure a) shows a single eruption sequence, plotted time versus first deviation of pressure. However, there seems to be an increase in the intensity of bubble implosions towards an eruption. (d) shows a typical sequence of a bubble implosion, starting with a slight positive peak, followed by a larger pressure drop and following positive peaks, that are likely caused by traveling waves inside the pool.

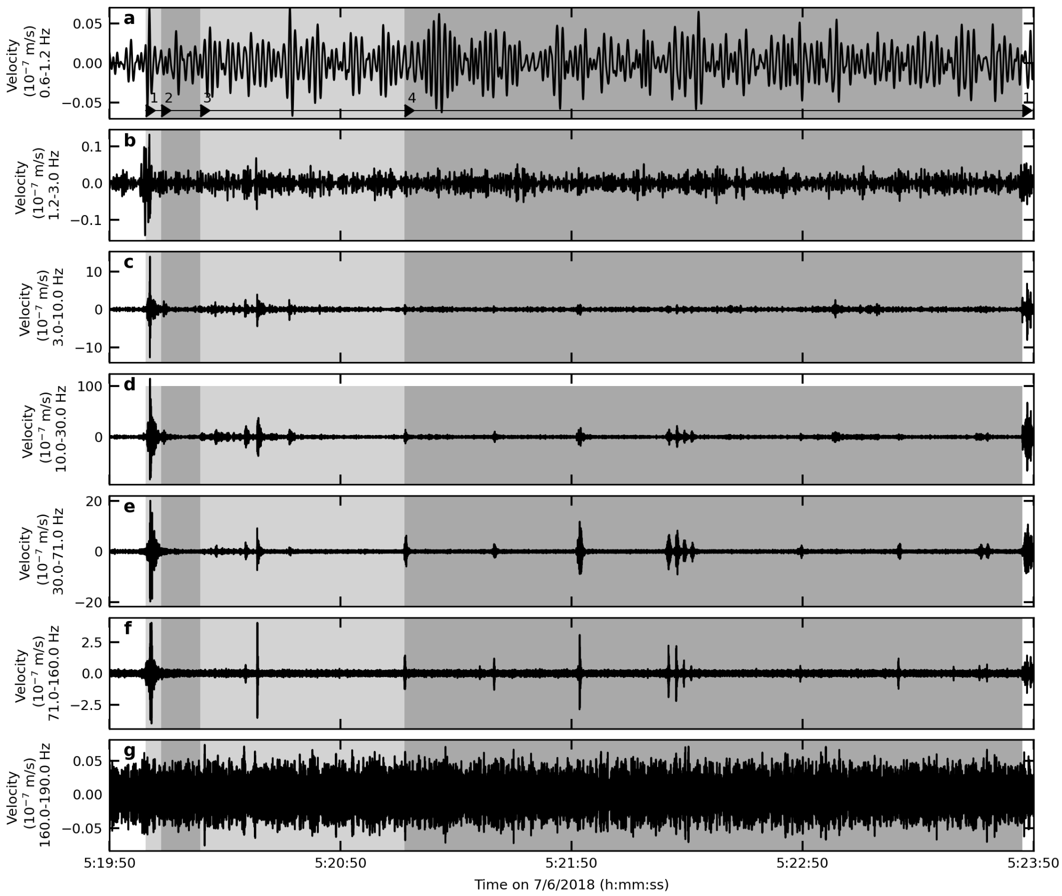

Figure A2. Seismic velocity of the North component at seismometer E2 in various frequency bands. We filtered (a) 0.6 to 1.2 Hz, (b) 1.2 to 3 Hz, (c) 3 to 10 Hz, (d) 10 to 30 Hz, (e) 30 to 71 Hz, (f) 71 to 160 Hz and (g) 160 to 190 Hz. Phases 1 to 4 are highlighted in grey.

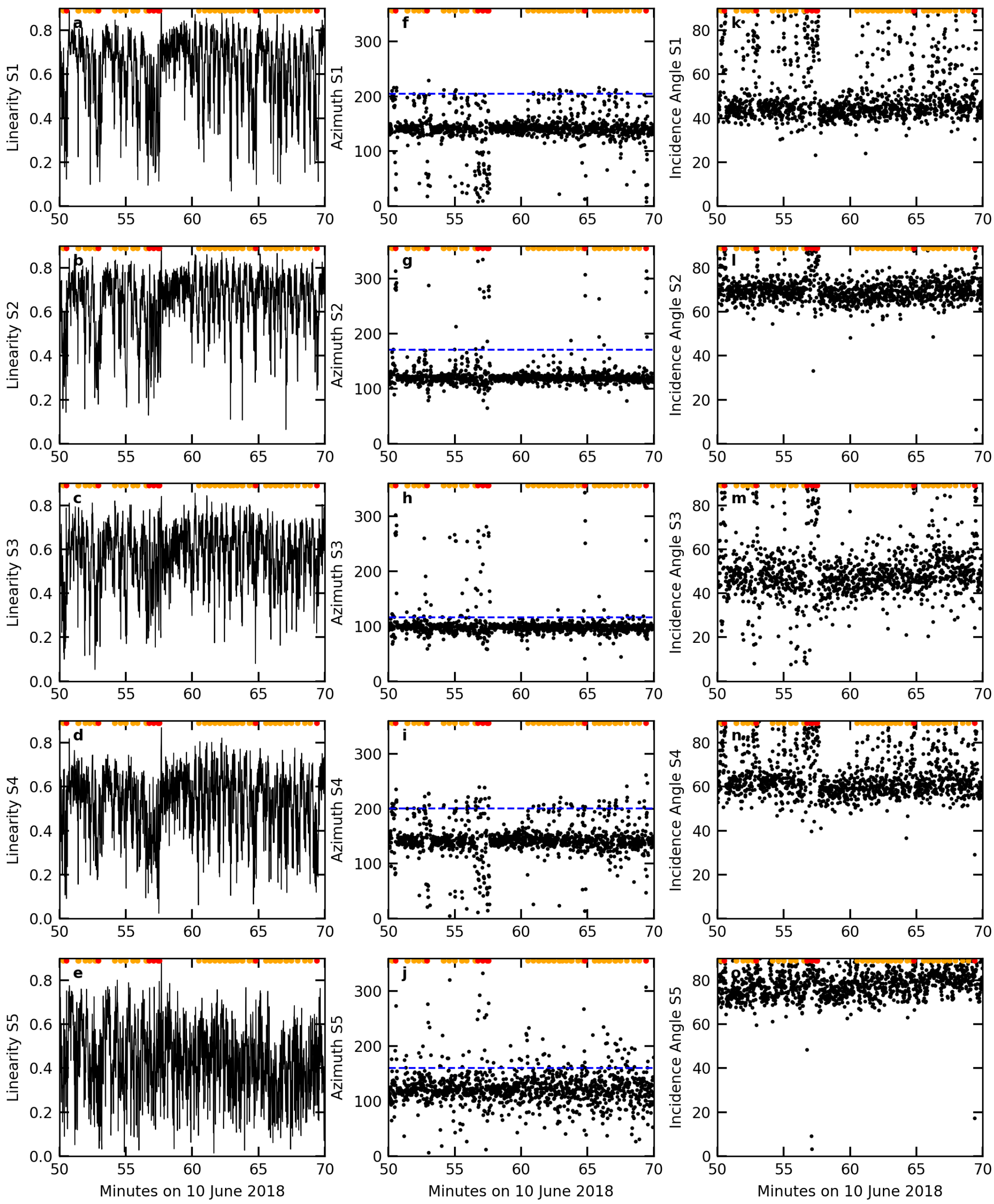

Figure A3. Direction derived from three components of the ground motion at S1 to S5 used as input for source location in Fig. 4. (a-e) Linearity, where 1 is linear particle motion. Red dots indicate eruptions, orange dots peaks in Phase 4. (f-j) Azimuth, where horizontal, blue dashed line indicates azimuth of the conduit. (k-o) Apparent incidence angle, where $90^{\circ}C$ indicates horizontal arrival.

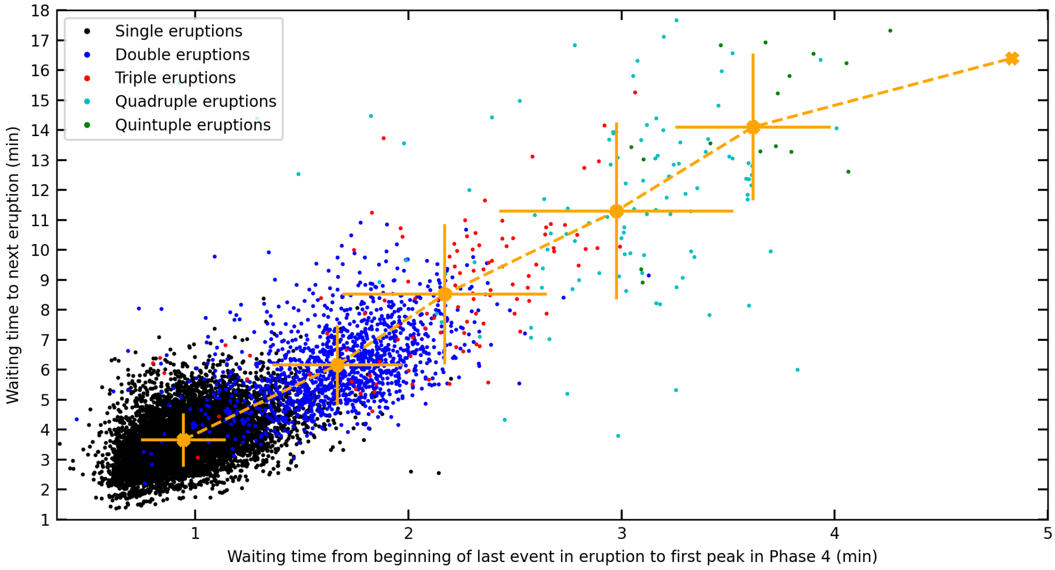

Figure A4. Waiting times from the last event within one set of eruptions to the first bubble implosion at depth in Phase 4 in comparison to t_{after} as published by Eibl et al. (2020). Plot shows 9512 single eruptions (black), 1359 double eruptions (blue), 108 triple eruptions (red), all 103 quadruple eruptions (cyan), all 17 quintuple eruptions (green) and the sextuple eruption. Average waiting times marked with yellow cross. ±1 standard deviation is marked by orange lines. Vertical lines from Eibl et al. (2020).

Han, W. S., Lu, M., McPherson, B. J., Keating, E. H., Moore, J., Park, E., … Jung, N. H. (2013). Characteristics of CO 2 -driven cold-water geyser, Crystal Geyser in Utah: Experimental observation and mechanism analyses. *Geofluids*, *13*(3), 283–297. doi: 10.1111/gfl.12018

Heimann, S., Kriegerowski, M., Isken, M., Cesca, S., Daout, S., Grigoli, F., … Dahm, T. (2017). *Pyrocko - An open-source seismology toolbox and library. V. 0.3* (Tech. Rep.). GFZ. doi: 10.5880/GFZ.2.1.2017.001

Hurwitz, S., & Shelly, D. R. (2017). Illuminating the Voluminous Subsurface Structures of Old Faithful Geyser, Yellowstone National Park. *Geophysical Research Letters*, *44*(20), 10,328–10,331. doi: 10.1002/2017GL075833

James, M. R., Lane, S. J., & Chouet, B. A. (2006). Gas slug ascent through changes in conduit diameter: Laboratory insights into a volcano-seismic source process in low-viscosity magmas. *Journal of Geophysical Research: Solid Earth*, *111*(5), 1–25. doi: 10.1029/2005JB003718

Jaupart, C., & Vergniolle, S. (1988). Laboratory models of Hawaiian and Strombolian eruptions. *Nature*, *331*, 9–12.

Karlstrom, L., Hurwitz, S., Sohn, R., Vandemeulebrouck, J., Murphy, F., Rudolph, M. L., … McCleskey, R. B. (2013). Eruptions at Lone Star Geyser, Yellowstone National Park, USA: 1. Energetics and eruption dynamics. *Journal of Geophysical Research: Solid Earth*, *118*(8), 4048–4062. doi: 10.1002/jgrb.50251

Karyono, K., Obermann, A., Lupi, M., Masturyono, M., Hadi, S., Syafri, I., … Mazzini, A. (2017). Lusi, a clastic-dominated geysering system in Indonesia recently explored by surface and subsurface observations. *Terra Nova*, *29*(1), 13–19. doi: 10.1111/ter.12239

Kedar, S., Kanamori, H., & Sturtevant, B. (1998). Bubble collapse as the source of tremor at Old Faithful Geyser. *Journal of Geophysical Research*, *103*(B10), 24283–24299. doi: 10.1029/98JB01824

Kedar, S., Sturtevant, B., & Kanamori, H. (1996). Origin of Harmonic Tremor at Old Faithful Geyser. *Nature*, *379*, 708–711.

Kieffer, S. W. (1984). Seismicity at Old Faithful Geyser: An isolated source of geothermal noise and possible analogue of volcanic seismicity. *Journal of Volcanology and Geothermal Research*, *22*, 59–95.

Megies, T., Beyreuther, M., Barsch, R., Krischer, L., & Wassermann, J. (2011). ObsPy - what can it do for data centers and observatories? *Annals of Geophysics*, *54*(1), 47–58. doi: 10.4401/ag-4838

Munoz-Saez, C., Manga, M., Hurwitz, S., Rudolph, M. L., Namiki, A., & Wang, C. Y. (2015). Dynamics within geyser conduits, and sensitivity to environmental perturbations: Insights from a periodic geyser in the El Tatio geyser field, Atacama Desert, Chile. *Journal of Volcanology and Geothermal Research*, *292*, 41–55. Retrieved from `http://dx.doi.org/10.1016/j.jvolgeores.2015.01.002` doi: 10.1016/j.jvolgeores.2015.01.002

Munoz-Saez, C., Namiki, A., & Manga, M. (2015). Geyser eruption intervals and interactions: Examples from El Tatio, Atacama, Chile. *Journal of Geophysical Research : Solid Earth*, *120*, 7490–7507. doi: 10.1002/2015JB012364

Namiki, A., Muñoz-Saez, C., & Manga, M. (2014). El Cobreloa: A geyser with two distinct eruption styles. *Journal of Geophysical Research: Solid Earth*, *119*(8), 6229–6248. doi: 10.1002/2014JB011009

Nishimura, T., Ichihara, M., & Ueki, S. (2006). Investigation of the Onikobe geyser, NE Japan, by observing the ground tilt and flow parameters. *Earth, Planets and Space*, *58*(12), 21–24.

Rinehart, J. S. (1965). Earth tremors generated by Old Faithful Geyser. *Science*, *150*(3695), 494–496. doi: 10.1126/science.150.3695.494

Rinehart, J. S. (1968). Seismic Signatures of Some Icelandic Geysers. *Journal of Geophysical Research*, *73*(14), 4609–4614.

Rudolph, M. L., Manga, M., Hurwitz, S., Johnston, M., Karlstrom, L., & Wang, C. Y. (2012). Mechanics of old faithful Geyser, Calistoga, California. *Geophysical Research Letters*, *39*(24), 1–5. doi: 10.1029/2012GL054012

Torfason, H. (1985). The Great Geysir. *Geysir Conservation Committee, Reykjavik*, 23.

Torfason, H. (1995). *Strokkur (in Icelandic)* (Tech. Rep.). Reykjavik: Orkustofnun.

Vandemeulebrouck, J., Roux, P., & Cros, E. (2013). The plumbing of Old Faithful Geyser revealed by hydrothermal tremor. *Geophysical Research Letters*, *40*(10), 1989–1993. doi: 10.1002/grl.50422

Vandemeulebrouck, J., Sohn, R. A., Rudolph, M. L., Hurwitz, S., Manga, M., Johnston, M. J. S., . . . Murphy, F. (2014). Eruptions at Lone Star geyser, Yellowstone National Park, USA: 2. Constraints on subsurface dynamics. *Journal of Geophysical Research : Solid Earth*, *119*, 8688–8707. doi: 10.1002/2014JB011526

Walter, T. R., Jousset, P., Allahbakhshi, M., Witt, T., Gudmundsson, M. T., & Hersir, P. (2020). Underwater and drone based photogrammetry reveals structural control at Geysir geothermal field in Iceland. *Journal of Volcanology and Geothermal Research*, *391*(106282). doi: 10.1016/j.jvolgeores.2018.01.010

Wang, C.-Y., & Manga, M. (2010). Earthquakes and Water. In *Earthquakes and water, lecture notes in earth sciences* (Vol. 114, pp. 117–123). Springer-Verlag Berlin Heidelberg. doi: 10.1007/978-3-642-00810-8_7

Wu, S. M., Lin, F. C., Farrell, J., & Allam, A. (2019). Imaging the Deep Subsurface Plumbing of Old Faithful Geyser From Low-Frequency Hydrothermal Tremor Migration. *Geophysical Research Letters*, *46*(13), 7315–7322. doi: 10.1029/2018GL081771

Wu, S. M., Ward, K. M., Farrell, J., Lin, F. C., Karplus, M., & Smith, R. B. (2017). Anatomy of Old Faithful From Subsurface Seismic Imaging of the Yellowstone

Upper Geyser Basin. *Geophysical Research Letters*, *44*(20), 10,240–10,247. doi: 10.1002/2017GL075255

Zhang, J. Y., Yan, C., & Huang, X. X. (2009). Edge detection of images based on improved sobel operator and genetic algorithms. In *Proceedings of 2009 international conference on image analysis and signal processing, iasp 2009* (pp. 32–35). doi: 10.1109/IASP.2009.5054605